

N 93 - 26478

Effect-specific analysis of propagation parameters

G. Ortgies, F. Rücker, F. Dintelmann and R. Jakoby
Forschungsinstitut der Deutschen Bundespost Telekom
Darmstadt, Germany

Abstract

Results of propagation measurements with the satellite OLYMPUS carried out at 12.5, 20 and 30 GHz at the Research Center of the Deutsche Bundespost Telekom will be discussed. In particular, attenuation, scintillation and depolarization measurements will be analyzed with special emphasis on frequency scaling of the various effects.

1 Introduction

Currently, the Research Center of the Deutsche Bundespost is participating in propagation experiments using the three beacons at 12.5, 20 and 30 GHz of the OLYMPUS satellite. In the higher frequency bands, clear-air effects such as gaseous absorption by oxygen and water vapour and attenuation caused by clouds have to be taken into account, which were of less importance in the 11/14-GHz band.

Besides these clear-air effects, rain attenuation is the most severe cause for signal degradation in satellite communications. Closely linked to it is depolarization where energy from one polarization state is cross-coupled into the orthogonal mode. Besides rain, ice has also been identified as a strong source for depolarization.

The various effects will be analysed with particular emphasis on an effect-specific frequency scaling behaviour.

2 Experiment

The receive facilities for the propagation measurements carried out at Darmstadt consist of a 1.8-m antenna for the reception of the B0 beacon at 12.5 GHz and a 3.7-m antenna to receive both, the B1 and B2 beacons at 20 and 30 GHz. The three OLYMPUS beacons are linearly polarized. In addition, the polarization state of B1 is switched between the horizontal and the vertical polarization state at a rate of 933 Hz. Hence, the full transfer matrix can be derived at 20 GHz.

In addition, meteorological equipment as well as radiometers are in operation at the receive site. The latter are used on one hand to derive the 0-dB levels for the beacon measurements, and on the other to distinguish between water vapour and cloud attenuation during non-rainy conditions, since they are more accurate than beacon measurements at low attenuations. Further experimental details can be found in [1].

3 Scintillations

Fluctuations of the refractive index in the troposphere give rise to amplitude scintillations. They manifest itself as fast fluctuations superimposed on the slowly varying attenuation caused by gaseous absorption, cloud and rain attenuation. An example is shown in Fig. 1 for the B2 beacon at 30 GHz.

Since the various attenuation effects and

scintillations scale differently in frequency, they need to be separated before an effect-specific analysis. The manner in which that can be accomplished, can be seen in Fig. 2, where power density spectra of scintillations observed during rain and clear-sky conditions are compared. It can be seen, that the spectra are very similar for Fourier frequencies above about 0.01 to 0.02 Hz. In this range they behave as theoretically expected with a constant power density up to a corner frequency around 0.1 Hz. Above this it decreases as $f^{-8/3}$. Slowly varying phenomena like rain attenuation give rise to the steep increase of the power density at very low frequencies. Thus, it is possible to separate the two effects by means of suitable filtering: a high-pass filter for scintillations and a low-pass filter for separating attenuation effects from the signal.

Having separated scintillation effects from the data, the crosscorrelation of scintillations measured with different antennas at different frequencies was investigated. The result is shown in Fig. 3 for a period of five minutes for the frequency pairs 12.5/20, 12.5/30 and 20/30 GHz. The highest cross-correlation factors (between 0.6 and 0.9) were found for data measured with the same antenna (20/30 GHz) whereas for the data measured with different antennas, the cross-correlation factors are significantly lower. Even values around zero were found, indicating complete decorrelation. Similar results have been observed at Virginia Tech in their scintillation diversity experiment [2]. Consequently it is not meaningful to derive event-based scintillation frequency scaling factors from scatterplots of simultaneously measured data at different frequencies.

Instead, cumulative distributions of the high-pass filtered time series data have been calculated on an event basis. They were found to be very similar for dry (scintillations during clear-sky conditions) and wet scintillations (in the presence of rain). In Fig. 4, an example is shown for wet scintillations. For all three beacons, the data

were found to be symmetrically distributed about the 50% probability level, which indicates that signal enhancement and attenuation are equally probable, a result which was also found for clear-sky scintillations [3].

From the cumulative distributions shown in Fig. 4, frequency scaling factors have been derived on an equiprobability basis. They are presented in Fig. 5 for the frequency pairs 12.5/20, 12.5/30 and 20/30 GHz. The scaling factors are found to be constant over the whole range of probabilities except for a small region around the 50% level, where signal excursions are very close to 0 dB and hence accuracy is very limited. Frequency scaling factors between 1.2 and 1.3 were found for 12.5 \rightarrow 20 and for 20 \rightarrow 30 GHz. For 12.5 \rightarrow 30 GHz, the scaling factor is about 1.4 to 1.5. These event-based results are in agreement with CCIR predictions[4]. No significant difference in the frequency scaling behaviour was found between rain dominated and clear-sky scintillations.

Since amplitude scintillations are Gaussian distributed around the mean beacon level for time intervals of the order of minutes, it appeared sensible to characterize them by their standard deviation. 1-min standard deviations have been calculated on-line from the high-pass filtered beacon signals. Until now, data have been gathered over a period of 25 months. Unfortunately, due to a gap in the data caused by the OLYMPUS failure in 1991, only a period of 12 consecutive months was statistically evaluated.

The cumulative statistics for clear-sky conditions, i.e. periods for which the 20-GHz attenuation was lower than 1 dB, are presented in Fig. 6 for 12.5, 20 and 30 GHz. Since the results for the vertically and horizontally polarized signals are virtually identical, only the vertically polarized component is shown at 20 GHz. As expected, the scintillation intensity increases with increasing frequency.

A similar analysis has been carried out for wet scintillations which are defined to occur

whenever the attenuation measured at 20 GHz exceeded 3 dB. The period which covers this attenuation range is about 0.2% of the total measuring time. The cumulative distributions of the standard deviations of the high-pass filtered data are presented in Fig. 7.

A comparison of the clear-sky results and those obtained for periods with rain attenuation indicate similar scintillation intensities for dry and wet scintillations. The probability, however, to exceed the same signal standard deviation as measured during clear-sky conditions is about a factor of 5 to 10 times higher during rain. This trend has been expected, since during rain, heavy clouds traversing the propagation path are always present, thus causing large refractive index fluctuations. During fair weather, however, clouds are found only for a much lower fraction of time.

Based on these one-year cumulative statistics, frequency scaling factors have been derived for wet and dry scintillations. The results are summarized in Table 1 together with CCIR predictions. They show that there is no significant difference in frequency scaling for dry and wet scintillations. The slightly higher value for wet scintillations when scaling from 12.5 to 30 GHz may be caused by an impairment due to wind gusts, which may cause short depointings of our 3.7-m antenna with the consequence of higher measured signal standard deviations.

Frequency scaling factors can be predicted according to the CCIR formula:

$$\frac{\sigma(f_1)}{\sigma(f_2)} = \left(\frac{f_1}{f_2} \right)^n \frac{g(f_2, H)}{g(f_1, H)} \quad (1)$$

where σ is the signal standard deviation at frequencies f_1 and f_2 . g is the antenna averaging factor and depends among other quantities on frequency and the height of the turbulent layer, H . In the CCIR prediction, a layer height of 1000 m and an exponent of $n = 0.578$ are assumed. Based on this procedure, predictions for frequency

scaling factors are included in Table 1, too. A comparison with the experimental results would indicate unreasonably large values for the height of the turbulent layer.

Therefore, a slight modification was applied to the CCIR formula. From the experimental data, the exponent n can be derived for the frequency pairs 12.5/20, 12.5/30 and 20/30 GHz independently. For the layer height assumed by CCIR (1000 m), three different values for n have been independently obtained using the experimental results of the three frequency pairs. However, when moving to a layer height of 1500 m, which is in good agreement with observations by Rucker and Dintelmann [5], the same value for the exponent n was found from the respective data of each frequency pair. Thus, a frequency dependence following a $f^{0.67}$ law fits best at least our scintillation data, as can be seen in Table 1.

4 Clear-air attenuation

After a discussion of high-pass filtered data, e.g. scintillation dominated effects, now low-pass filtered data will be discussed. When moving to higher frequencies, attenuation caused by the atmospheric gases oxygen and water vapour as well as attenuation due to clouds can no longer be neglected. Since these effects scale differently in frequency, the effect-specific attenuation contributions have been separated. For this investigation, radiometers were used, since they are more accurate at lower attenuations than beacon measurements.

The measured total attenuation at frequency f , $A_{total}(f)$, is a superposition of contributions from oxygen, $A_{oz}(f)$, water vapour, $A_{wv}(f)$, and clouds, $A_{cl}(f)$. If the oxygen attenuation is assumed to be constant, the contributions from water vapour and clouds can be calculated from simultaneous attenuation measurements carried out at different frequencies f_1 and f_2 by

solving this set of equations:

$$A_{total}(f_1) = A_{ox}(f_1) + A_{wv}(f_1) + A_{cl}(f_1) \quad (2)$$

$$A_{total}(f_2) = A_{ox}(f_2) + A_{wv}(f_2) + A_{cl}(f_2) \quad (3)$$

How this simple procedure works, can be seen in Fig. 8, in which the total attenuation and its contributions are presented for an interval of 3 hours. It can be seen that the slowly varying water vapour attenuation can be successfully separated from the liquid water attenuation caused by clouds traversing the propagation path. In combination with beacon measurements, the different contributions can be scaled separately to that beacon frequency, for which no radiometer data are available, in order to accurately determine the 0-dB level.

Once having separated the different contributions, statistics have been evaluated for periods, for which no rain attenuation occurred on the propagation path. The results are presented as cumulative distributions of the attenuation contributions for 20 GHz (Fig. 9) and 30 GHz (Fig. 10). As expected, because of the vicinity of the water vapour resonance band at 22.2 GHz, the water vapour attenuation was found to be higher at 20 GHz than the cloud attenuation. The picture is different at 30 GHz. Here, in about 40% of the time the cloud attenuation exceeds the water vapour attenuation. Cloud attenuation of up to 3 dB was found even without rain on the propagation path. This has to be taken into account when planning low-margin systems.

The statistics for the effect-specific different contributions can then be investigated separately, e.g. as input for modelling of clouds [6].

5 Rain attenuation

More severe than clear-air attenuation is attenuation caused by rain. In order to investigate instantaneous frequency scaling, in Fig. 11, low-pass filtered attenuation data

measured simultaneously at 12.5 and 30 GHz are presented in a scatterplot for three different rain events. A hysteresis-like effect can be seen in the data. The instantaneous frequency scaling factor changes not only during the event, but also from event to event. For comparison, the long-term CCIR scaling factor is shown as well.

A similar behaviour was also observed for the other two frequency pairs 12.5/20 GHz and 20/30 GHz. Since the effect is most pronounced for 12.5/30 GHz, this frequency pair will be used in the following discussion. Similar results were also observed at Virginia Tech in their 20/30-GHz data.

The following items have been investigated as possible causes for hysteresis: a variation of the drop size distribution [7,8] and the length of the path through the rain cell [7]. As a third item, antenna effects have been identified [7,9].

With the help of regression coefficients [10], the influence of different drop size distributions can be easily simulated for our experimental conditions. The results are within the shaded area in Fig. 12. A comparison with the experimental results indicates that a large variability can be explained in this way. In the discussion of depolarization effects, it can be seen in detail, that the structure of the rain cell undergoes changes during a rain event.

The influence of different path lengths is shown in Fig. 13. Here, the attenuation is calculated for the Laws/Parsons drop size distribution for effective path lengths between 2 and 8 km (shaded area). A comparison with the measurements indicates that part of the hysteresis might be caused also by changes of the effective path length, especially, when low attenuation frequency scaling factors are found.

If antennas with different beam widths are used, this might also cause hysteresis. The idea is that a rain cell which approaches the propagation path causes an earlier attenuation increase on the propagation path of the

antenna with the larger beam width. Later the attenuation ratio is determined by the weighted ratio of the common volumes. This ratio changes when the rain cell moves and, therefore, might cause hysteresis.

Calculations which simulated this scenario for our experimental conditions were carried out for different shapes of rain cells. In order to give an impression of the order of magnitude of the hysteresis effect, two examples are presented in Fig. 14. The first example represents a Lorentz-shaped rain cell which moves with constant velocity parallel to the earth's surface through the propagation path. The resulting attenuation ratios are found within the shaded area in Fig. 14 (I). As a consequence, hysteresis can be explained this way and the effect is not negligible. An interesting result of these simulations is that different directions of this s-shaped hysteresis curve, which have been observed in the measurements, can be simulated by changing the direction of the moving rain cell relative to the antenna bearing.

In the second example, a fixed rain cell is simulated in which the rain drops are falling down with constant velocity and in which the components of the velocity parallel to the earth's surface are zero. The temporal development of the rain rate was characterized by an asymmetrical triangular function. The result is given by the shaded area (II) in Fig. 14. Again, hysteresis effects can be seen. Taking the two examples together, once again, a large area of hysteresis can be explained by antenna effects.

Many other situations have been investigated and more or less pronounced hysteresis effects were found. Only in cases with a high degree of symmetry, e.g., when the rain cell moves perpendicular to the propagation path, no hysteresis was observed.

What are the consequences of hysteresis effects for instantaneous frequency scaling, e.g. in up-link power control? To answer this question, the probability distribution of hysteresis-caused errors has been calculated

for measurements a of one-year period for the attenuation range 5 to 10 dB at 20 GHz. In the first case, the error is defined by the difference of the measured attenuation at 30 GHz and the CCIR-predicted data from 20 GHz measurements (Fig. 15). The respective distribution is shifted towards negative values indicating that the measured attenuations are greater than the predicted ones. Errors of more than ± 4 dB occur.

An attempt was made to take the information of the attenuations measured at 12 GHz into account for the prediction. It was found that the errors are of the same order of magnitude. Only the maximum of the error distribution is shifted towards a mean value of 0 dB.

In a third attempt, the structure of the rain cell was taken into account. In particular, the information on the differential attenuation at 20 GHz was used in the prediction. In this case, the large errors became smaller, but errors of ± 2 dB are obvious, indicating that a variation of the rain cell structure might not be the only reason for hysteresis.

6 Depolarization

Closely linked to rain attenuation is depolarization. OLYMPUS with its switched beacon at 20 GHz offers the possibility to get a deeper insight into the causes of depolarization. They will be discussed on an event basis.

In Fig. 16, crosspolar discrimination, XPD, is plotted versus copolar attenuation for three attenuation events measured during one day in September 1990. Attenuations were found up to 14 dB. It can be seen, that there is no clear relationship between attenuation and XPD. For comparison, theoretical curves for rain depolarisation are depicted for two different drop size distributions, Marshall/Palmer and Sekhon/Srivastava. Only for high attenuation, the predictions converge. At lower

attenuations, large deviations occur, indicating that rain is not the only depolarization cause.

Reasons for depolarization are differential attenuation and differential phase shift. In the following, the frequency scaling behaviour of these parameters will be discussed.

The relationship between the differential attenuation and the concurrently measured copolar attenuation is shown in Fig. 17. It can be seen that the main trend of the measured data can be well represented by theoretical predictions. As in the previous and in the following examples, the solid and the dotted curves represent predictions from the Marshall/Palmer and the Sekhon/Srivastava drop size distributions, respectively. Nevertheless, there are significant deviations, especially at low attenuations. Since here the differential attenuations are small, it is assumed that spherical rain drops are predominant up to attenuations of about 7 dB at 20 GHz.

A rough estimate indicates that the differential attenuation is about 10% of the copolar attenuation.

A scatterplot of simultaneously measured differential attenuation and differential phase is presented in Fig. 18. Here no clear correlation can be seen. Only a small fraction of the data agree with model calculations. It is assumed that in this case rain is the cause for depolarization. In regions in which large differential phase shifts are measured concurrently with only small differential attenuations, ice is assumed to be the major cause for depolarization. In most cases, the phase difference between nominally horizontally and vertically polarized signals is positive which can be explained by horizontally aligned ice plates. In case of negative differential phase shifts, the particles are assumed to be vertically aligned which can be caused e.g. by electric fields or wind gradients.

Scaling XPD in frequency is not straight

forward. Whereas the differential attenuation scales in the same way as rain attenuation, for the differential phase, neither a pronounced correlation with the differential attenuation nor with the measured copolar attenuation was found. Since measurements of the differential phase are available only at 20 GHz, there are no direct means to derive the frequency scaling behaviour for this quantity. However, this relation can be derived indirectly. To this end, the copolar attenuation and differential attenuation measured at 20 GHz were scaled to 30 GHz and the differential phase which was needed at 30 GHz to end up at the measured XPD at this frequency was calculated. The so determined differential phase at 30 GHz is plotted in Fig. 19 versus the measured differential phase at 20 GHz. A clear relationship can be seen between these two quantities.

For comparison, the expected relationship for different drop size distributions is also shown. It can be recognized that only part of the XPD event is caused by rain. Instead, it is assumed that the part of the XPD event associated with high differential phase was caused by ice.

The experimental results for scaling XPD in frequency are presented in Fig. 20 whereas theoretical curves for different drop size distributions and ice are shown in Fig. 21 for comparison. In general, it can be stated that scaling of XPD is approximately independent of the cause for depolarization.

So far XPD frequency scaling for a fixed polarization tilt angle has been discussed. If in addition XPD data have to be scaled to another polarization tilt angle or to circular polarization, the effective canting angle, e.g. the angle between the polarization plane of the electromagnetic wave and the characteristic plane of the propagation medium, is a key parameter. The canting angle can be derived from dual polarization measurements as well. An example is presented in Fig. 22. It has been found that the mean value of the prevailing canting angle is 21 deg. This is exactly the polarization tilt angle at our

receive site, indicating that the rain drops are oriented either horizontally or vertically.

Once knowing the effective canting angle, XPD values can be scaled to any other polarization tilt angle or to circular polarization.

7 Conclusions

Results of propagation measurements carried out at the Research Center of the Deutsche Bundespost Telekom have been presented. Attenuation, scintillation and depolarization measurements have been analyzed with particular emphasis on frequency scaling of the effect-specific signal contributions.

It has been shown that for dry and wet scintillations the same frequency scaling ratios are applicable. A modified CCIR scaling procedure fits well our experimental results. Possible causes for hysteresis effects in rain attenuation measurements as well as their impact on instantaneous frequency scaling have been discussed. With the depolarization measurements at 20 GHz, the nature of the depolarizing medium can be identified. It has been shown, how differential attenuation, differential phase and XPD scale in frequency.

References

- [1] F. Dintelmann, G. Ortgies and F. Rücker: Earth-station requirements and description of a complete facility, Proc. OLYMPUS Utilisation Conference, Vienna, 227-233 (1989)
- [2] T. Pratt, D. Sweeney and F. Haidara: Olympus propagation experiment at Virginia Tech - Recent results for frequency scaling and scintillation, Proc. of the 16th Meeting of Olympus Propagation experimenters, Aveiro, 99-131 (1991)
- [3] G. Ortgies and F. Rücker: Frequency scaling of slant-path amplitude scintillations, Proc. URSI Commission F Symposium, Ravenscar (1992)
- [4] CCIR Report 718-3: Effects of tropospheric refraction on radiowave propagation, Geneva (1990)
- [5] F. Rücker and F. Dintelmann: Effect of antenna size on OTS signal scintillations and their seasonal dependence, Electronics Letters, 21(4), 143-145 (1985)
- [6] F. Dintelmann and G. Ortgies: Semiempirical model for cloud attenuation prediction, Electronics Letters, 25(22), 1487-1488 (1989)
- [7] G. Ortgies, F. Rücker and F. Dintelmann: Some aspects of attenuation frequency scaling, URSI Commission F Symposium, London, Canada (1991)
- [8] D.G. Sweeney, T. Pratt and C.W. Bostian: Hysteresis effects in instantaneous frequency scaling of attenuation at 20 and 30 GHz links, Electronics Letters 28(1), 76-78 (1992)
- [9] F. Rücker, G. Ortgies and F. Dintelmann: Aspects of attenuation frequency scaling, Proc. of the First OPEX Workshop, Noordwijk, WPP 24, 3.3.1-3.3.12 (1991)
- [10] E. Damosso: Dependence of specific rain attenuation and phase shift on electrical, meteorological and geometrical parameters, Proc. of Symp. on Advanced Satellite Communications Systems, Genoa, ESA SP-138, 219-225 (1978)

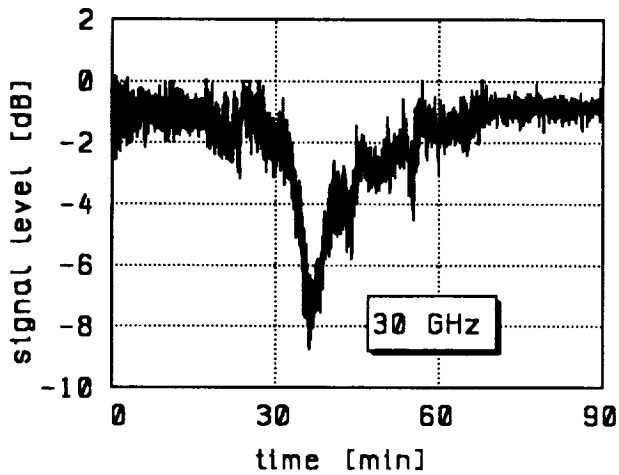


Figure 1: Scintillations superimposed on rain attenuation at 30 GHz.

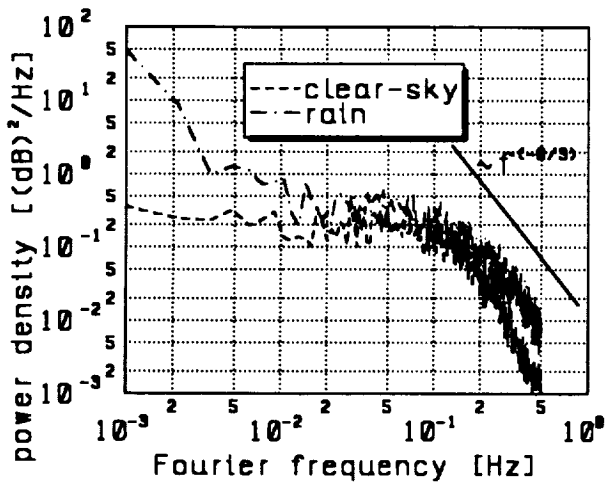


Figure 2: Spectral power density of the 20-GHz signals for clear-sky conditions and during rain.

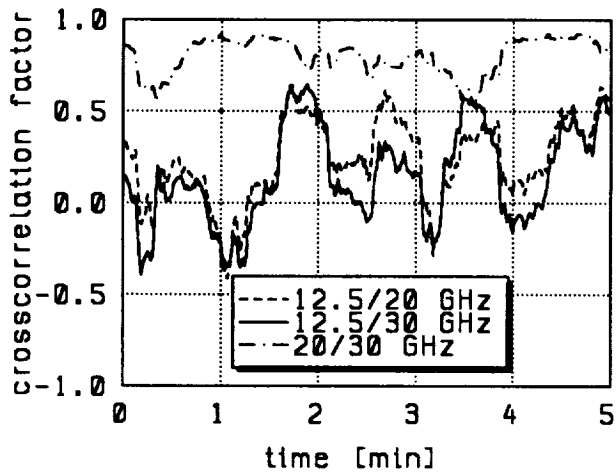


Figure 3: Crosscorrelation analysis of signals measured at 12.5, 20 and 30 GHz with different antennas.

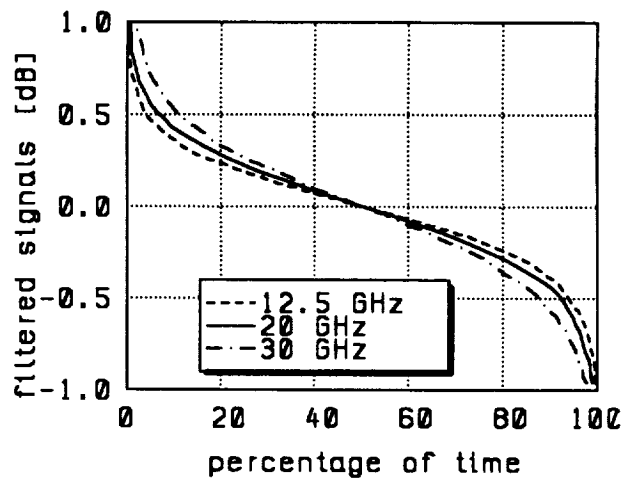


Figure 4: Cumulative distributions of high-pass filtered data at 12.5, 20 and 30 GHz during rain.

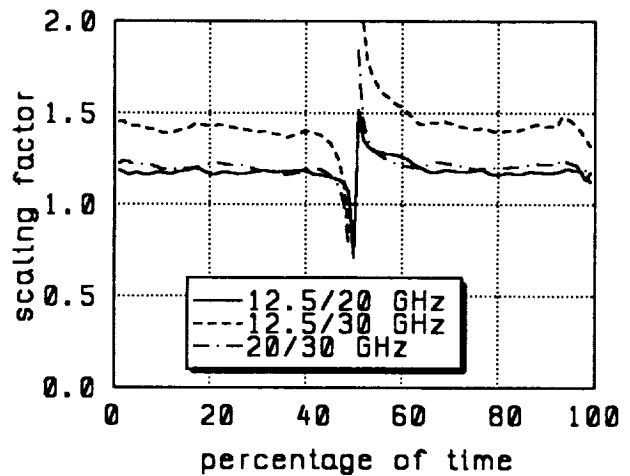


Figure 5: Frequency scaling factors derived from Fig. 4 on an equiprobability basis.

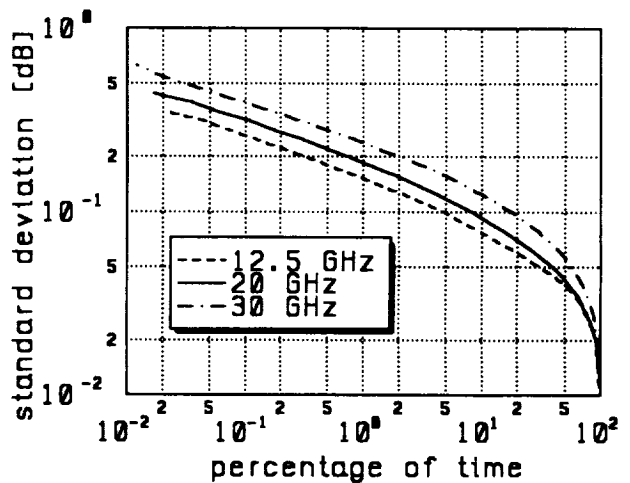


Figure 6: Cumulative distributions of 1-min standard deviations during clear-sky conditions.

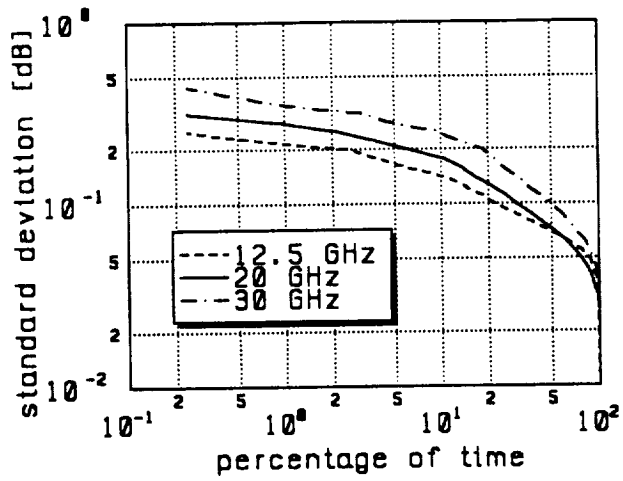


Figure 7: Cumulative distributions of 1-min standard deviations during rain.

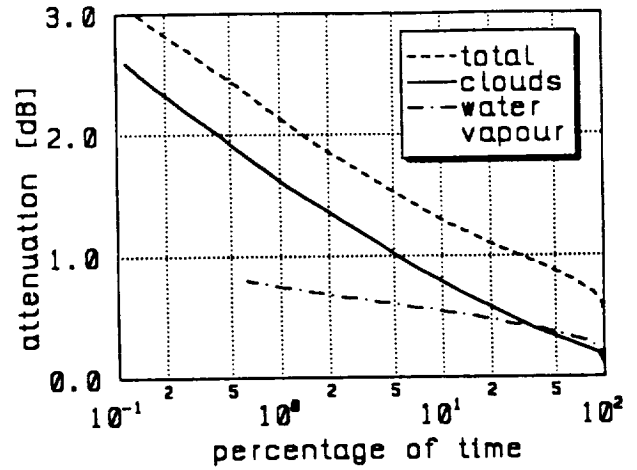


Figure 10: Cumulative distributions of total attenuation at 30 GHz and contributions from clouds and water vapour.

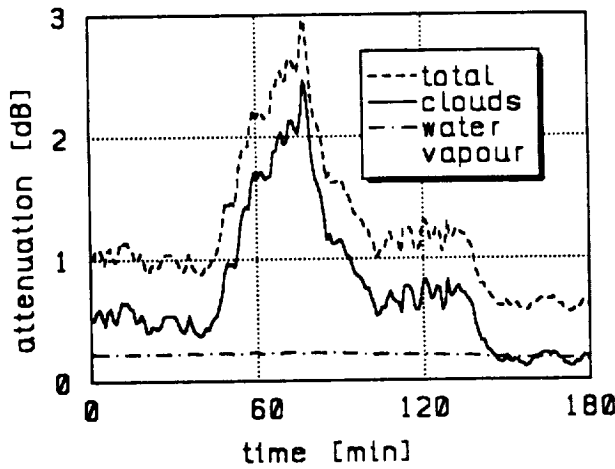


Figure 8: Separation of attenuation contributions from clouds and water vapour at 30 GHz.

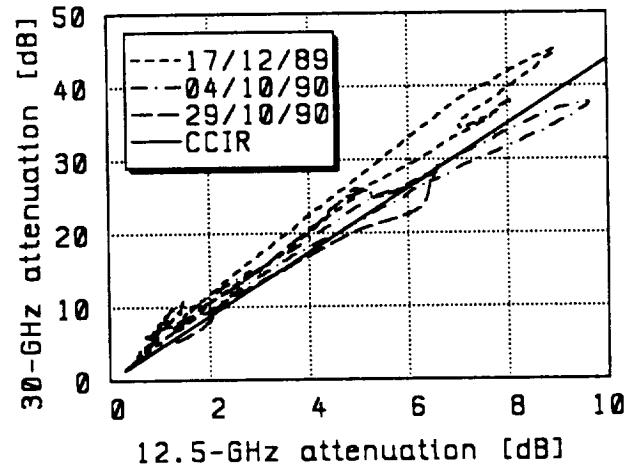


Figure 11: Scatterplots of simultaneously measured attenuations at 12.5 and 30 GHz.

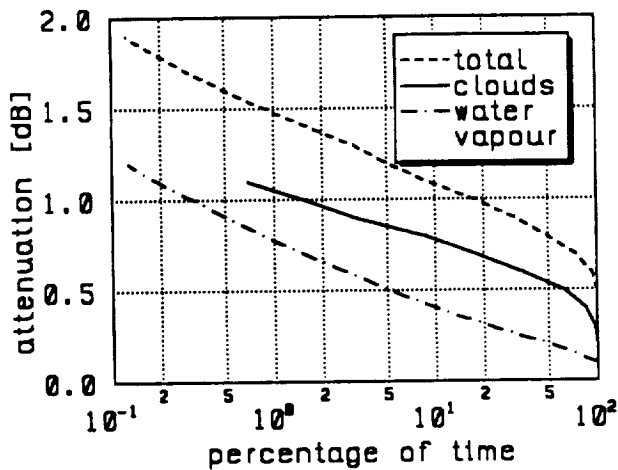


Figure 9: Cumulative distributions of total attenuation at 20 GHz and contributions from clouds and water vapour.

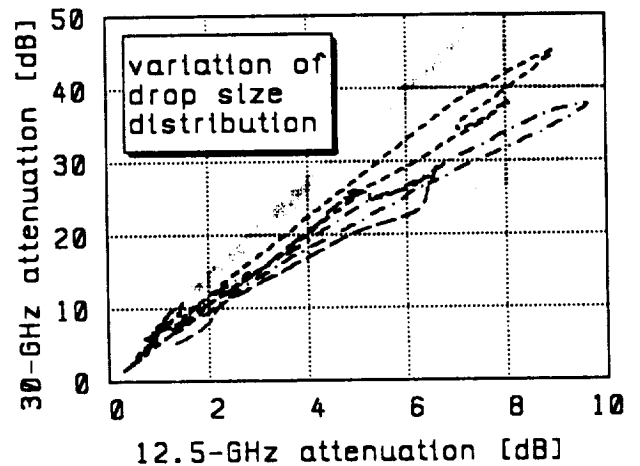


Figure 12: Hysteresis caused by a variation of the drop size distribution.

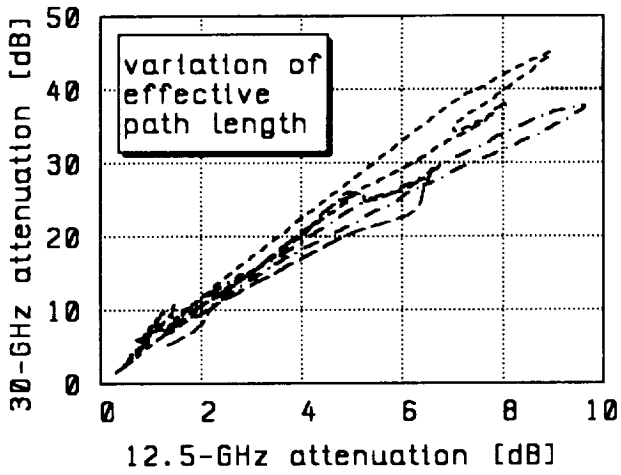


Figure 13: Hysteresis caused by a variation of the effective path length.

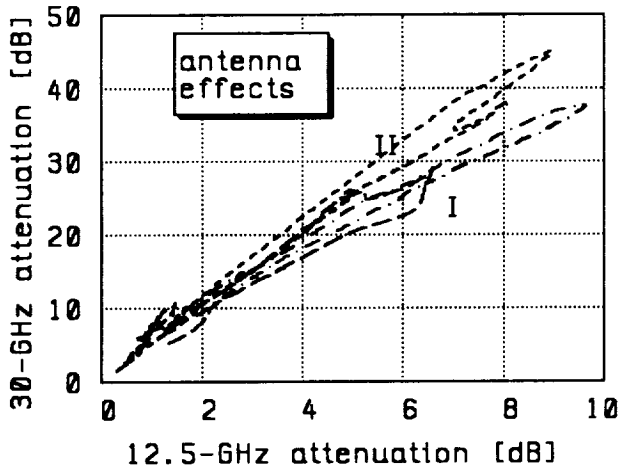


Figure 14: Hysteresis caused by a antenna effects.

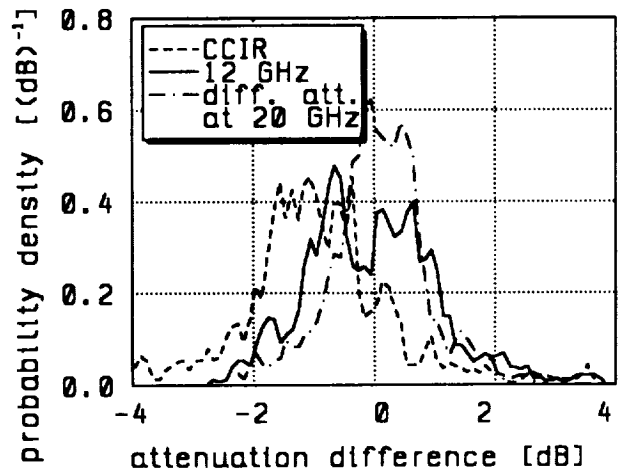


Figure 15: Distribution of hysteresis caused errors based on measurements of a one-year period.

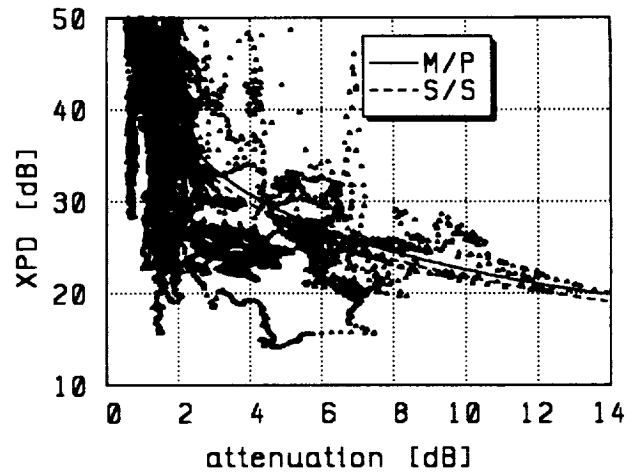


Figure 16: Simultaneously measured attenuation and XPD at 20 GHz.

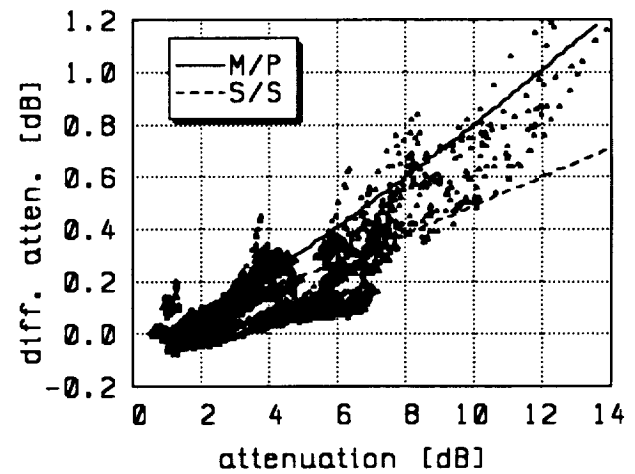


Figure 17: Simultaneously measured attenuation and differential attenuation at 20 GHz.

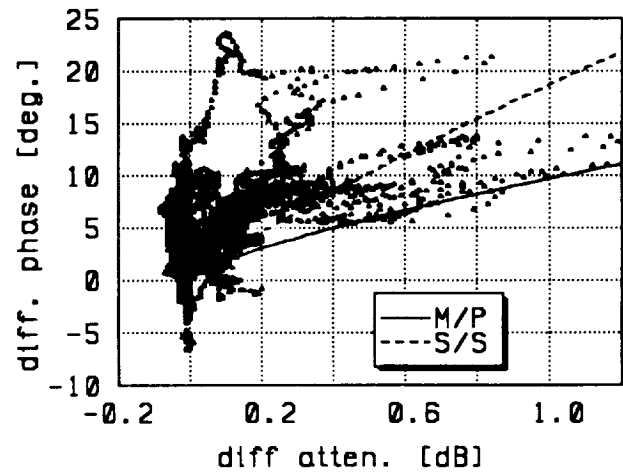


Figure 18: Simultaneously measured differential attenuation and differential phase shift at 20 GHz.

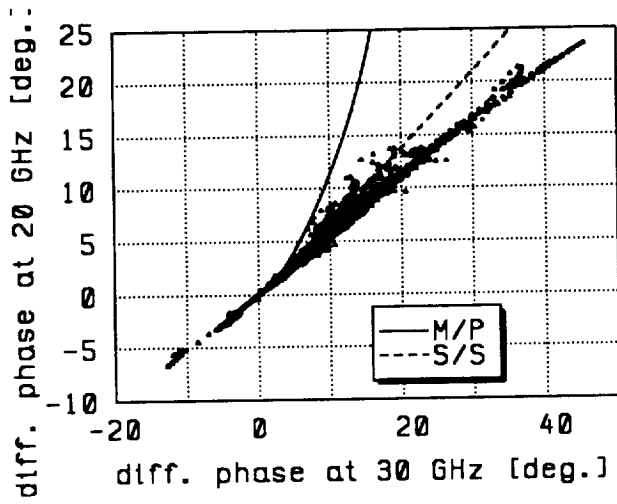


Figure 19: Frequency scaling of differential phase shift.

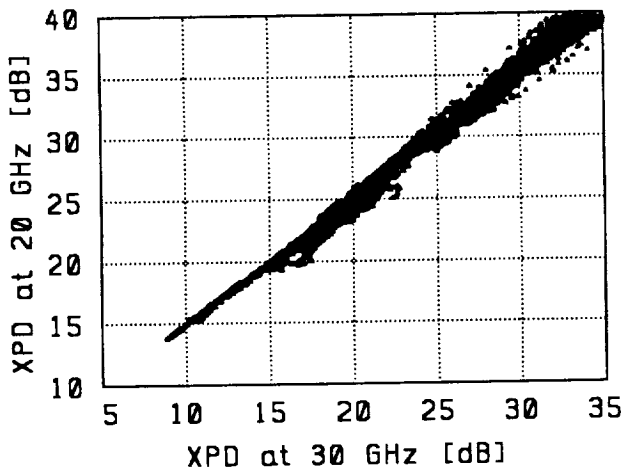


Figure 20: Simultaneously measured XPD at 20 and 30 GHz.

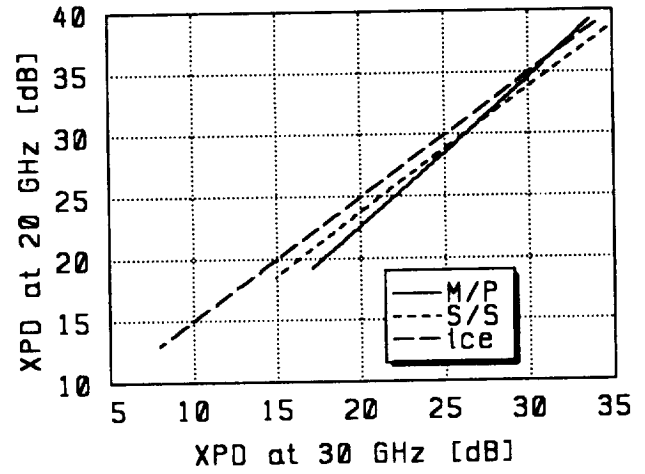


Figure 21: Theoretical relations between XPD at 20 and 30 GHz.

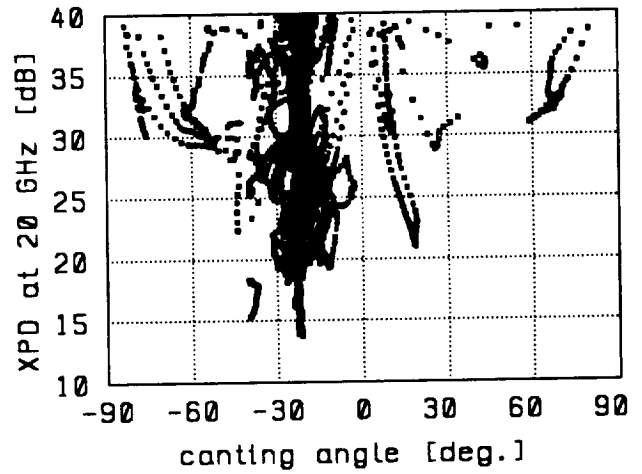


Figure 22: Effective canting angle versus XPD at 20 GHz.

frequency GHz	measured		CCIR 500 m	CCIR 2000 m	CCIR modified 1500 m
	clear-sky	rain			
12.5→20	1.23	1.25	1.06	1.24	1.23
12.5→30	1.58	1.65	1.31	1.55	1.59
20→30	1.29	1.30	1.23	1.26	1.29

Table 1: Scintillation frequency scaling factors.